Computed Tomography (CT)–Based Analysis of Regional Lung Ventilation

15

Andrea Aliverti, Francesca Pennati, and Caterina Salito

15.1 Regional Ventilation: First Studies with Radioactive Gases and Preliminary Findings

Classical studies on regional ventilation with lobar spirometry [1, 2] and radioactive gases [3, 4] demonstrated regional differences in the distribution of ventilation, preferentially toward the lower lung zones. The first quantitative results are reported by West and Dollery [3], measuring the removal rate of oxygen15-labeled carbon dioxide after a single breath of the radioactive gas by external counting, and by Ball et al. [4], who measured regional ventilation by xenon scintigraphy by relating the lung count rate after a single breath to that after isotope equilibration throughout the lung. These preliminary findings have demonstrated that the lower portion of the lung is better ventilated and receives a much greater fraction of the total pulmonary blood flow and that the middle and lower portions of the lung are better ventilated on the left than on the right during deep inspiration. Subsequent works from Milic-Emili and coworkers [5, 6] attributed this behavior to the combined effect of the gradient of pleural pressure and the static volume-pressure relation of the lung. They have demonstrated that there is a vertical gradient of pleural pressure which causes nondependent portion of the lung to be relatively more expanded than the dependent. Moreover, these more distended units at the top of the lung are on a flatter part of their pressure-volume curve than the smaller units at the bottom; thus, equal pressure increments produce smaller volume increments at the top than at the bottom of the lung (Fig. 15.1).

A. Aliverti, PhD (✉) • F. Pennati • C. Salito
Dipartimento di Elettronica, Informazione e Bioingegneria, Politecnico di Milano,
P.zza L. da Vinci, 32, Milano 20133, Italy
e-mail: andrea.aliverti@polimi.it

A. Aliverti, A. Pedotti (eds.), *Mechanics of Breathing*,
DOI 10.1007/978-88-470-5647-3_15, © Springer-Verlag Italia 2014

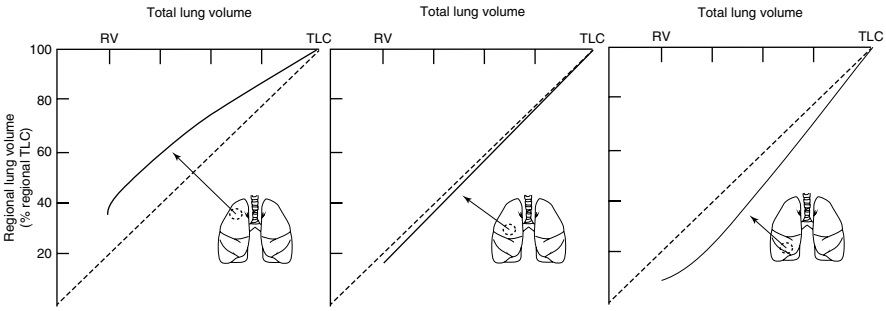

Fig. 15.1 Regional lung volume (expressed as percentage of TLCr) with respect to overall lung volume (expressed as percentage of TLC). From left to right, increasing distance from the top of the lung (apex) to the base

Multiple investigations followed these preliminary findings, and multiple imaging techniques have been developed for investigating regional ventilation. This chapter reviews the development of computed tomography in imaging regional lung ventilation.

15.2 Computed Tomography Imaging: Basic Principles

Computed tomography (CT) is currently the main imaging modality for diagnosing lung diseases. High-resolution CT scanners generate a three-dimensional view of the imaged organs with submillimeter resolution in axial sections. CT provides detailed information regarding the lung parenchyma and can delineate structures down to the level of the secondary pulmonary lobule, the smallest structure in the lung. It is particularly useful for image-based diagnosis since alteration of the lung anatomy, caused by a disease, can be clearly seen in a thin-slice CT image [7].

15.2.1 The Evolution of CT

CT was introduced in the early 1970s and has revolutionized not only diagnostic radiology but also the whole field of medicine. The introduction of spiral CT in the early 1990s constituted a fundamental evolutionary step in the development and ongoing refinement of CT imaging techniques. Until then, the examination volume had to be covered by subsequent axial scans in a "step-and-shoot" mode. Axial scanning required long examination times because of the interscan delays necessary to move the table incrementally from one scan position to the next, and it was prone to misregistration of anatomic details (e.g., pulmonary nodules) because of the potential movement of relevant anatomic structures between two scans (e.g., by patient motion, breathing, or swallowing). The most important advancement in these CT scanners has been the implementation of X-ray detectors that are physically separated in the z-axis direction and enable simultaneous acquisition of

multiple slices of the patient's anatomy. Key benefits of multidetector computed tomography (MDCT) systems are faster scan speed, improved through-plane resolution, and better utilization of the available X-ray tube power. MDCT also expanded into new clinical areas, such as CT angiography of the coronary arteries with the addition of ECG gating capability [8, 9]. An 8-slice CT system, introduced in 2000, enabled shorter examination times but no improved spatial resolution (thinnest collimation 8×1.25 mm). In 2001, 16-slice CT systems became commercially available, with collimations of 16×0.5, 16×0.625, or 16×0.75 mm and faster gantry rotation (down to 0.42 s and later 0.375 s) [10]. In 2004, all major CT manufacturers introduced MDCT systems with simultaneous acquisition of 64 slices at 0.5, 0.6, or 0.625 mm collimated slice width and further reduced rotation times (down to 0.33 s). GE, Philips, and Toshiba aimed at increasing volume coverage speed by using detectors with 64 rows, in this way providing 64 collimated 0.5 or 0.625 mm slices with a total z-coverage of 32 or 40 mm. Siemens used 32 physical detector rows in combination with a z-flying focal spot to simultaneously acquire 64 overlapping 0.6 mm slices with a total z-coverage of 19.2 mm, with the goal of pitch-independent increase of through-plane resolution and reduction of spiral artifacts [11]. With 64-slice CT systems, CT scans with isotropic submillimeter resolution became feasible even for extended anatomic ranges. In 2007, an MDCT system with 128 simultaneously acquired slices was introduced based on a detector with 64×0.6 mm collimation and double z-sampling by means of a z-flying focal spot. Recently, simultaneous acquisition of 256 slices has become available, with a CT system equipped with a 128-row detector (0.625 mm collimated slice width) and z-flying focal spot. Clinical experience with 64-, 128-, or 256-slice CT indicates that the performance level of MDCT has reached a level of saturation, and mere adding of even more detector rows will not by itself translate into increased clinical benefit [10].

The applied dose is ultimately the limiting factor for the improvement of image quality and increase in isotropic resolution. In order to make best diagnostic use of the applied dose, sophisticated dynamic dose adaptation techniques to patient size and geometry have been developed. A recent study [12] showed that the use of additional tin filtration in the high-energy X-ray beam of a dual-source CT system provided several benefits for dual-energy CT applications, including a similar or lower radiation dose compared with the conventional single energy CT, increased dual-energy contrast, and improved image quality of dual-energy material-specific (e.g., virtual noncontrast) images. Moreover, the virtual noncontrast imaging of dual-energy CT has a potential to reduce the radiation dose by omitting precontrast scanning [13].

15.2.2 Radiation Dose

The increasing use of CT has sparked concern over the effects of radiation dose on patients, particularly for those who had repeated CT scans. The effective dose [14] from a CT scan on average is ~10 mSv [15]. The health risks, mainly cancer

induction and mortality, from this level of radiation dose have been considered in detail by an expert Committee of the National Research Council of the National Academies of the USA and published as BEIR VII Phase 2 report [16].

Various measures are used to describe the radiation dose delivered by CT scanning, the most relevant being absorbed dose, effective dose, and CT dose index (or CTDI). The absorbed dose is the energy absorbed per unit of mass and is measured in grays (Gy). One gray equals 1 J of radiation energy absorbed per kilogram. The organ dose (or the distribution of dose in the organ) largely determines the level of risk to that organ from the radiation. The effective dose, expressed in sieverts (Sv), is used for dose distributions that are not homogeneous (which is always the case with CT); it is designed to be proportional to a generic estimate of the overall harm to the patient caused by the radiation exposure. The effective dose allows for a rough comparison between different CT scenarios but provides only an approximate estimate of the true risk. For risk estimation, the organ dose is the preferred quantity. Organ doses can be calculated or measured in anthropomorphic phantoms [17]. Historically, CT doses have generally been (and still are) measured for a single slice in standard cylindrical acrylic phantoms [18]; the resulting quantity, the CT dose index, although useful for quality control, is not directly related to the organ dose or risk [19]. The radiation doses to particular organs from any given CT study depend on a number of factors. The most important are the number of scans, the tube current and scanning time in milliampseconds (mAs), the size of the patient, the axial scan range, the scan pitch (the degree of overlap between adjacent CT slices), the tube voltage in the kilovolt peaks (kVp), and the specific design of the scanner being used. Many of these factors are under the control of the radiologist or radiology technician. Ideally, they should be tailored to the type of study being performed and to the size of the particular patient, a practice that is increasing but is by no means universal [20].

Efforts and measures to reduce noise can be initiated by the examiner by critically considering the indication and the choice of scanning protocols and parameters for any CT examination and by the manufacturer during the development of dose-efficient systems, together with special technical measures and methods. Patient dose has to be kept "as low as reasonably achievable" (ALARA principle), as postulated by the International Commission on Radiological Protection [21].

15.2.3 CT Images of the Lung

Image gray scale is measured in Hounsfield units (HU), an arbitrary linear scale defined as zero for water and approximately −1,000 for air, that results convenient for lung imaging as the density of any lung volume may be considered as a combination of air, at −1,000 HU, and "tissue" (cells, blood, collagen, water), at 0 HU. As the lung volume increases, gas volume increases while tissue remains constant. Thus, the overall lung density decreases as the lung expands. Changes in CT density provide accurate measurements of regional and global lung air and tissue volume as well as an indication of the heterogeneity of lung expansion.

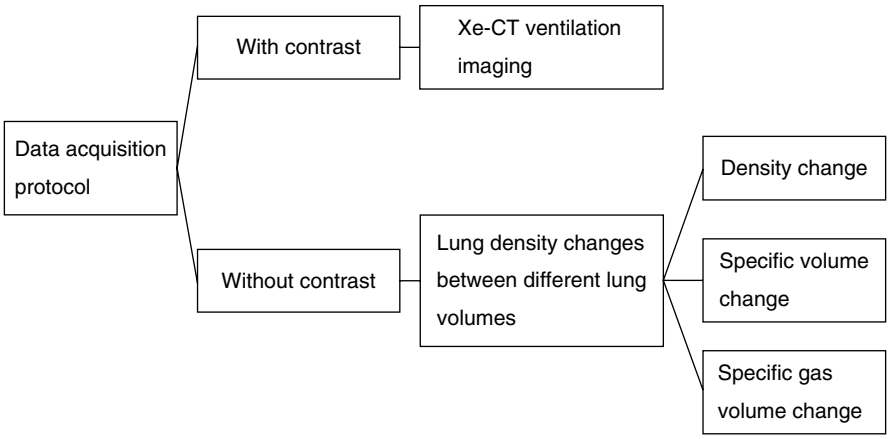

Fig. 15.2 CT-based ventilation imaging

These principles are at the basis of functional pulmonary measurements. Tracer techniques for ventilation using a radio-dense gas have the advantage that the accumulation of tracer gas during regular breathing should follow the same gas transport principles as respiratory gases. Density-based methods and registration-based techniques require the assumption that the decrease in CT density due to region expansion is caused by only gas influx (Fig. 15.2).

15.3 Xenon-CT Ventilation Imaging

The use of xenon as a contrast agent for ventilation imaging was pioneered by Gur et al. [22], but only recently it has been updated, refined, and validated as a research tool in animal experiments [23–26]. Xenon is a nonradioactive gas with higher radiodensity than air, resulting in a linear CT density increase with increasing gas concentration. Two Xe-enhanced computed tomography (Xe-CT) techniques for imaging regional ventilation have been developed: single-breath and multi-breath technique. The single-breath technique [23] is performed by asking the subject to take a single breath of a high Xe concentration mixture and comparing Xe-enhanced with unenhanced images. Regional ventilation is directly assessed by the Xe enhancement. Multi-breath technique measures regional pulmonary ventilation from the wash-in and wash-out rates of the Xe gas, as measured in serial CT scans (Fig. 15.3).

The temporal changes in CT density enhancement produced during the wash-in and wash-out phases in any region can be exponentially fitted, providing a time constant equal to the inverse of the local ventilation per unit volume, i.e., specific ventilation in the hypothesis of a single-compartment model (Fig. 15.3).

The quantification of Xe-CT is affected by the variable CT attenuation of the lung parenchyma of the scanned subject due to different lung volumes on sequential images, thus restricting the first studies to animal model [22–26]. Xenon-enhanced

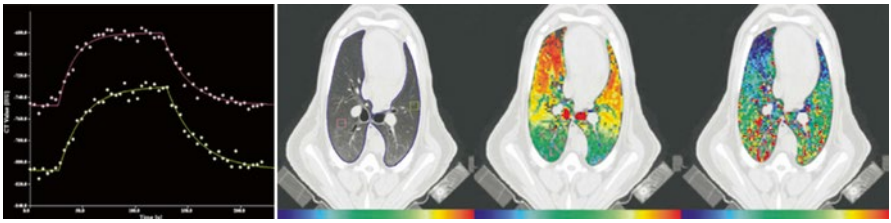

Fig. 15.3 Xe-CT with density-time curve for two ROIs of a mechanically ventilated sheep (*left*) and map of regional air content (% air, *middle*) and specific ventilation (sec^{-1}, *right*) (Modified from Simon [31])

dual-energy CT has been introduced by Chae et al. [27] to overcome this limitation, as the Xe component can be calculated from the dual-energy CT on the basis of the material decomposition theory without additional unenhanced acquisition. With this approach clinical studies have been performed, indicating dual-energy Xe-CT as a promising tool for detecting abnormal pulmonary ventilation [27–30].

The use of Xe-CT has a number of limitations. The anesthetic properties of xenon, that limit its use in humans to a maximum concentration around 30–35 % [31, 32], limit the maximum CT density enhancement achievable. Xenon is moderately soluble in blood and tissue, and this has been proposed to affect background density level and alveolar accumulation rates [26]. Nevertheless, Hoag et al. [33] demonstrated that Xe uptake has no significant impact on the measured lung density-time curve. Another important limitation is that Xe-CT is time and radiation intensive. Each study requires 20 up to 70 repeated respiratory-gated axial images at each location, with repeated scans for volumetric coverage [31].

15.4 Lung Aeration and Recruitment

Over the past 20 years, many experimental and clinical studies have described the different CT morphological patterns of acute lung injury (ALI). The pioneering CT studies of Gattinoni and coworkers [34–36] have demonstrated that ALI is characterized by significant regional differences in lung aeration and alveolar recruitment with tidal volume and positive end-expiratory pressure, and that these regional differences determine the local response to different ventilation strategies.

On the basis of the basic CT principles and assuming lung-specific weight equal to 1, the volume of gas in any lung region of interest can be related to regional density as

$$\frac{\text{volume}_{\text{gas}}}{\text{volume}_{\text{gas}} + \text{volume}_{\text{tissue}}} = \frac{\text{meanHU}}{\text{HU}_{\text{gas}} - \text{HU}_{\text{water}}}$$

where $\text{volume}_{\text{gas}}$ and $\text{volume}_{\text{tissue}}$ are, respectively, the volume of gas and tissue within the region of interest, meanHU is the mean density value of the region, and

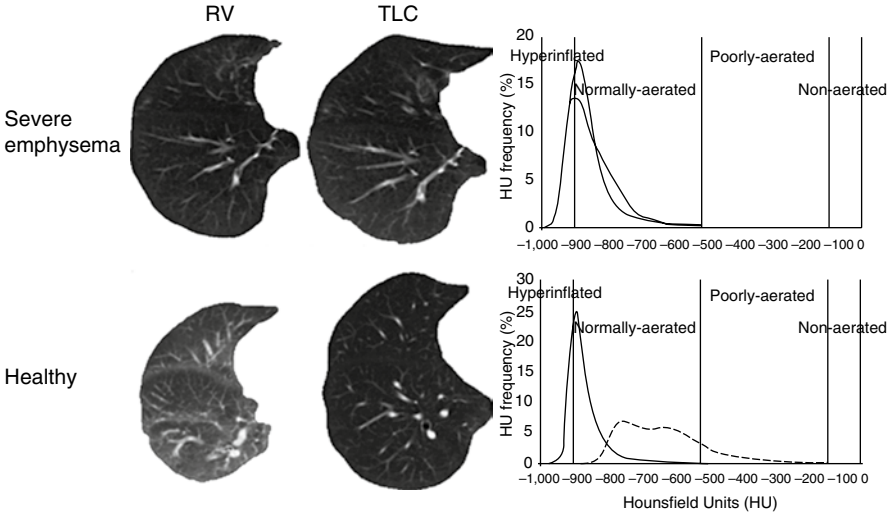

Fig. 15.4 The lung compartments, as defined by Hounsfield units, in severe emphysema (*top*) and in normal condition (*bottom*) for the right lung at RV (*dashed line*) and TLC (*solid line*)

HU_{gas} and HU_{water} are, respectively, the density value of gas (−1,000 HU) and water (0 HU).

From this simple relation, gas volume, tissue volume, and weight and the ratio gas/tissue are derived [35–37]:

$$\text{Volume}_{\text{gas}_\text{ROI}} = \text{volume}_{\text{ROI}}\left(\text{meanHU}_{\text{ROI}} / -1{,}000\right)$$

$$\text{Tissue_weight}_{\text{ROI}} = \text{volume}_{\text{ROI}}\left(1-\left(\text{meanHU}_{\text{ROI}} / -1{,}000\right)\right)$$

Gattinoni et al. [38] proposed to divide the lung in different compartments according to their degree of aeration, from unaerated (from 0 to −100 HU) to poorly aerated (from −101 to −500 HU), normally aerated (from −501 to −900 HU), and hyperinflated (from −901 to −1,000 HU) (Fig. 15.4). Taking CT scans under different conditions, it is therefore possible to determine the alveolar recruitment and ventilation distribution. Alveolar recruitment, defined as the amount of gas entering unaerated tissue when the applied airway pressure increases, is estimated as the unaerated tissue change, expressed in grams, under different ventilatory conditions [38]. The distribution of ventilation is obtained as the alveolar inflation change between end inspiration and end expiration [39].

More recently, Dougherty et al. [40, 41] introduced a new method for mapping regional aeration within the lung: by applying deformable image registration at CT images acquired in breath-hold at residual volume and total lung capacity in patients with severe emphysema. Deformable image registration consists in finding the spatial mapping between corresponding voxels in two images. Therefore, the quantitative change of each voxel across different states of inflation can be determined by

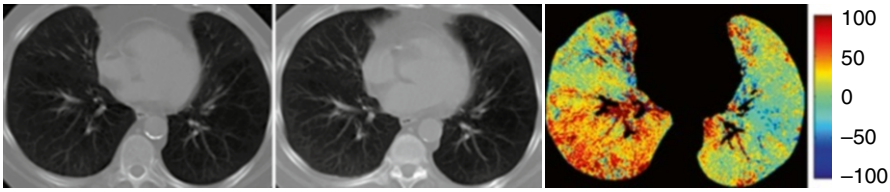

Fig. 15.5 Thoracic CT at total lung capacity (TLC, *left*), residual volume (RV, *middle*), and map of Hounsfield units difference (*right*) computed as $HU_{RV} - HU_{TLC}$ after registering RV onto TLC

image subtraction, and the resulting difference map can be used to visualize and quantify regional pulmonary air trapping [40, 41] (Fig. 15.5).

15.5 Specific Volume Change

Simon [42] proposed to quantify regional mechanical properties of the lung from CT density changes between pairs of breath-hold CT images. In the hypothesis that volume change occurs only because of the addition of fresh gas into the lung with inspiration, regional specific compliance (sC; compliance per unit volume) can be measured from CT images acquired at two different pressures, from the changes in local fraction of air content (F) with changes in inflation pressure (ΔP) as

$$\mathrm{sC} = \left(F_2 - F_1\right) / \left(F_1\left(1 - F_2\right)\Delta P\right)$$

Specific compliance measured between 0 and 15 cm H_2O airway pressures has shown good agreement to Xe-CT in two anesthetized mechanically ventilated dogs [42]. Thus, it has been proposed as a surrogate for regional ventilation, introducing the term specific volume change (sVol; change in volume divided by initial gas volume) [31]. Using the relationship between CT density (HU) and air fraction (F), specific volume change can be calculated from the density change as

$$\mathrm{sVol} = 1{,}000\left(\mathrm{HU}_2 - \mathrm{HU}_1\right) / \left(\mathrm{HU}_1\left[\mathrm{HU}_2 + 1{,}000\right]\right)$$

However, this relationship is nonlinear and dependent on both initial region density and the magnitude of the density change. As shown in Fig. 15.6, there can be large differences in sVol for the same ROI density change depending on initial region density, illustrating why CT density change is a poor correlate for regional ventilation [42].

Guerrero et al. [43, 44] pioneered the use of sVol maps from four-dimensional CT in lung tumor patients in order to optimize the radiation therapy treatment planning, avoiding well-ventilated pulmonary regions which could reduce treatment-related complications (Fig. 15.7). The main advantage of 4D-CT functional imaging in lung tumor patients is that it requires no additional dose or extra cost to the patient as 4D-CT is routinely acquired through thoracic radiotherapy treatment planning. We would like to clarify some terminological inaccuracy arising from

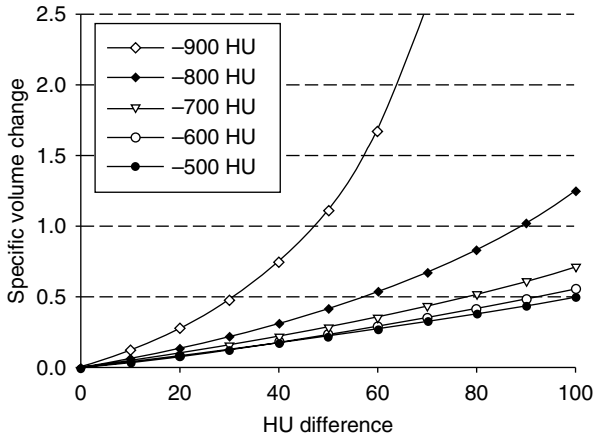

Fig. 15.6 Specific volume change as a function of Hounsfield units difference at different initial densities

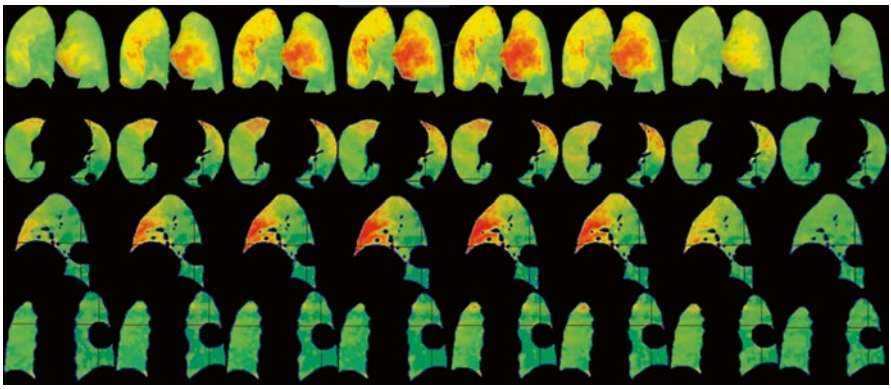

Fig. 15.7 The 4D-CT ventilation image set of a patient with lung tumor from end expiration up to end inspiration and again to end expiration (from *left* to *right*). Each image was paired with the maximum expiration phase to compute the change in specific volume change with respect to the maximum expiration. Volume-rendering (*first row*), transversal (*second row*), sagittal (*third row*), and frontal views (*fourth row*) are reported

Guerrero et al. [44], where the term "specific ventilation" was associated to specific volume change, which was introduced as a surrogate for regional ventilation [31]. Since then, several studies [45–48] developed in the field of radiotherapy reported the term "ventilation images" referring to maps of specific volume change obtained from 4D-CT lung images. Maps of specific volume change were compared to Xe-CT ventilation images in an anesthetized sheep [49] and to single-photon emission tomography (SPECT) ventilation images in lung tumor patients [45]. Results demonstrated high Dice similarity coefficient in regions with matched perfusion-ventilation defects but an overall low similarity and a low correlation coefficient between the two imaging techniques [45]. Yamamoto et al. [46] investigated specific volume change in patients with emphysema by correlating specific volume change defects with the disease. Further studies quantified the dosimetric impact of

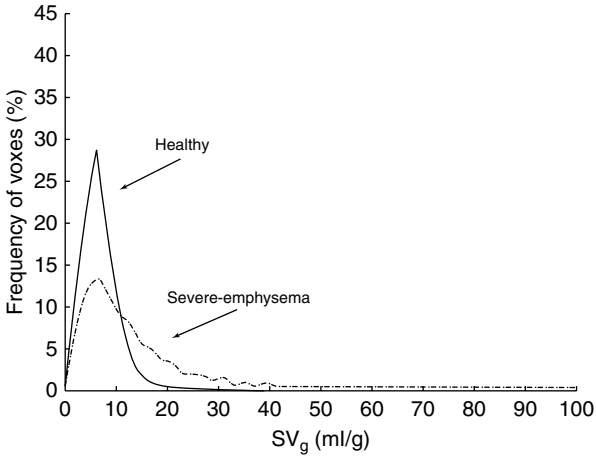

Fig. 15.8 The frequency distribution of the CT voxels expressed as gas volume per gram of tissue at TLC. The solid line represents the healthy subjects; the dashed line represents the group with severe emphysema. These two distributions are different from each other ($p<0.001$)

4D-CT functional imaging on treatment planning to avoid well-ventilated lung regions during radiation therapy [47]. Vinogradskiy et al. [48] used functional maps calculated from weekly 4D-CT data to study ventilation change throughout the radiation therapy.

15.6 Specific Gas Volume

Specific volume of gas (SV_g) is defined as volume of gas per gram of tissue (ml/g) and is derived pixel by pixel from CT images of lung density by converting the HU value to a measure of specific volume, which is a more physiologically meaningful measure [50–52]. SV_g can be calculated pixel by pixel as

$$SV_g = \text{specific volume}_{(\text{tissue\&gas})} - \text{specific volume}_{(\text{tissue})}$$

where specific volume (expressed in ml/g) is the inverse of density (g/ml).

The specific volume of the lung (tissue and gas) is measured from the CT as

$$SV_{(\text{tissue\&gas})}(\text{ml/g}) = \frac{1,024}{\text{HU}(\text{mg/ml}) + 1,024}$$

where the specific volume of tissue was assumed to be equal to 1/1.065 = 0.939 ml/g [53].

This method was first introduced by Coxson et al. [51, 54] in studies assessing regional lung volumes from CT scans. Figure 15.8 shows the frequency distribution for the quantity of gas per gram of tissue, at TLC, present in each CT voxel in a group of healthy subjects ($N=10$) and in a group of patients with severe emphysema ($N=10$).

The healthy lung shows a symmetrical distribution with mean, median, and mode values closely similar. The severe emphysema group has a flattened distribution that is markedly shifted and skewed to the right.

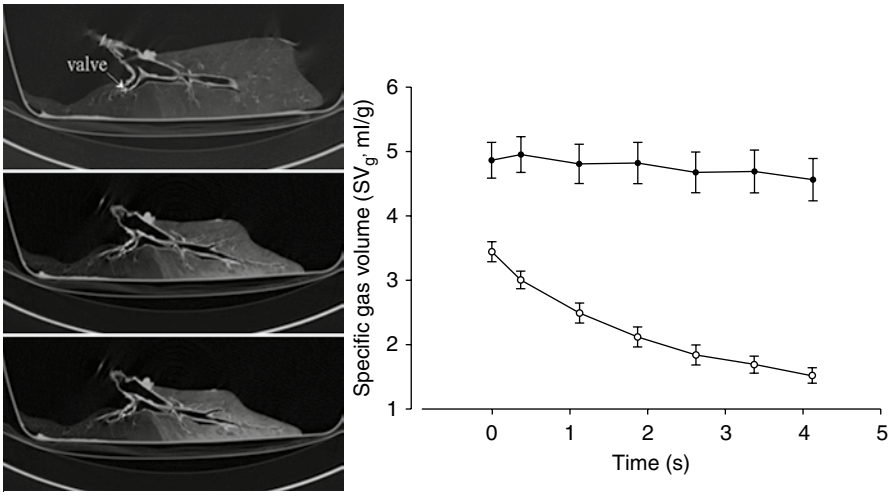

Fig. 15.9 (**a**) Dynamic CT scans of a longitudinal slice during 4.5 s of exhalation in a pig lung (three representative images from *top* to *bottom*, 2.25 s between images). The presence of trapped gas is clearly visible and stable in the obstructed lobe (upper lobe) in which the obstruction was created by inserting the one-way endobronchial exit valve (clearly visible in the upper lobar bronchus). (**b**) Graph of time-evolving SV_g of the obstructed and the unobstructed lobe (Modified from Salito et al. [52])

In recent studies performed on an animal model of airway obstruction [52] and in the emphysematous lungs in vivo [55], Salito et al. showed that CT-determined $SV_{g,r}$ is sensitive to the extent of regional trapped gas (Fig. 15.9).

Therefore, SV_g can be used to evaluate the extent of gas trapping on a regional base. SV_g is expected to change smoothly as a function of lung volumes. Total specific gas volume of the lung (SV_g) represents an average of all regional specific gas volume ($SV_{g,r}$). A reasonable hypothesis is that in the emphysematous lung, if there are regions where $SV_{g,r}$ varies little with lung volume (V) so that the slope of a plot of $\Delta SV_{g,r}$ versus overall ΔV is smaller than that for both lungs, there must be other regions where $\Delta SV_{g,r}/\Delta V$ is steeper indicating a greater than average decrease in $SV_{g,r}$ with decreasing V. In a normal lung there is no gas trapping above closing volume so that the spread of values of $\Delta SV_{g,r}/\Delta V$ should be small, whereas in emphysema the considerably larger set of slopes can potentially be used as a measure of inhomogeneous emptying (Fig. 15.10).

SV_g can be calculated for regions of interest, corresponding to different bronchopulmonary segments. This was done in healthy volunteers and emphysematous patients in whom CT images were taken at high and low lung volumes. Figure 15.11 shows two examples, one relative to a representative healthy subject and one showing the data of a patient with severe emphysema. In the healthy lung all bronchopulmonary segments show similar $\Delta SV_g/\Delta V$ slopes, while in emphysema the distribution of slopes is larger with more lung regions having low values of ΔSV_g,r/ΔV and other with higher values. The former can be considered as regions in which gas trapping is more pronounced and therefore more feasible for interventions aimed to reduce volume.

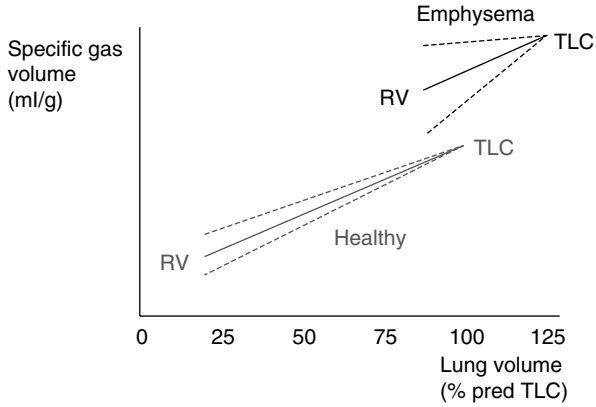

Fig. 15.10 Schematic representation of the expected relationship between variations of specific gas volume and lung volume: comparison between emphysema and healthy subjects

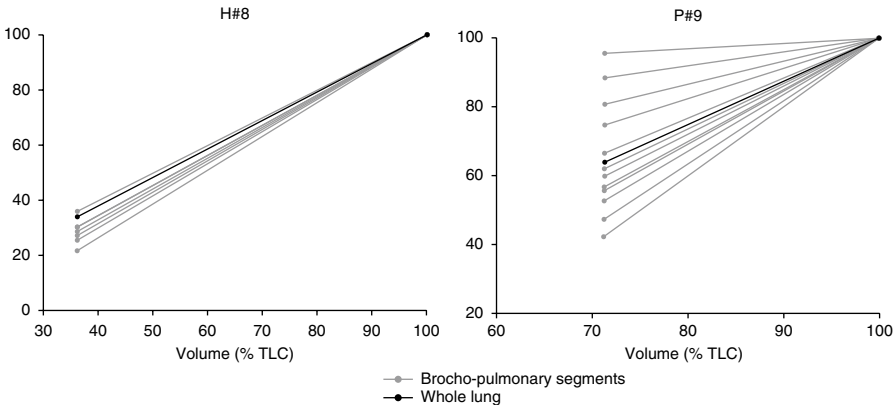

Fig. 15.11 Specific gas volume (SV_g, expressed as % $SV_{g,TLC}$) as function of the lung volume (expressed as %TLC volume) in a representative healthy subject (*left*) and in one patient with emphysema (*right*). *Gray lines*: segments connecting SV_g and volume values at TLC and RV in all bronchopulmonary segments. *Black lines*: segments connecting SV_g and volume values at TLC and RV in the whole lung

Recently, Aliverti et al. [56] introduced image registration to map regional lung function in terms of density and SV_g changes between different lung volumes in health and emphysema (Fig. 15.12) and showed that ΔSV_g is more homogeneously distributed within the lungs with no significant gravity dependence. Therefore, ΔSV_g maps, rather than ΔHU and sVol maps, have the advantage of minimizing the dependence of ventilation distribution on gravity. In other words, any heterogeneity has to be interpreted as the result of phenomena other than gravity, i.e., the disease.

These findings have clinical and physiological implications, not only in the assessment of the patient in the different stages of the disease but also to detect regional alterations in the lung function (e.g., gas trapping or collateral ventilation).

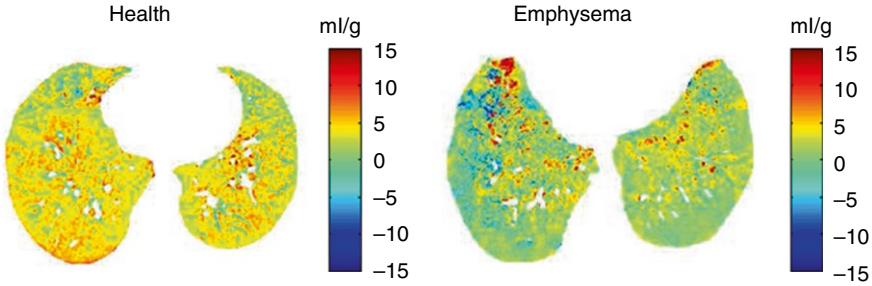

Fig. 15.12 Maps of specific gas volume change computed between total lung capacity and residual volume expressed in ml/g at the top diaphragm level of a representative healthy volunteer (*left*) and a representative patient with severe emphysema (*right*)

Such possibility would be extremely useful for planning and guiding interventions of bronchoscopic lung volume reduction surgery.

References

1. Martin CJ, Young AC (1956) Lobar ventilation in man. Am Rev Tuberc 73(3):330
2. Mattson SB, Carlens E (1955) Lobar ventilation and oxygen uptake in man; influence of body position. J Thorac Surg 30(6):676
3. West JB, Dollery CT (1960) Distribution of blood flow and ventilation-perfusion ratio in the lung, measured with radioactive CO2. J Appl Physiol 15(3):405–410
4. Ball WC, Stewart PB, Newsham LGS, Bates DV (1962) Regional pulmonary function studied with xenon133. J Clin Invest 41(3):519
5. Milic-Emili J, Henderson JA, Dolovich MB et al (1966) Regional distribution of inspired gas in the lung. J Appl Physiol 21:749–759
6. Bryan AC, Milic-Emili J, Pengelly D (1966) Effect of gravity on the distribution of pulmonary ventilation. J Appl Physiol 21:778–784
7. Webb RW, Muller N, Naidich DP (2009) High-resolution CT of the lung, 4th edn. Lippincott Williams & Wilkins
8. Kachelriess M, Ulzheimer S, Kalender W (2000) ECG-correlated image reconstruction from subsecond multi-slice spiral CT scans of the heart. Med Phys 27:1881–1902
9. Ohnesorge B, Flohr T, Becker C et al (2000) Cardiac imaging by means of electro—cardiographically gated multisection spiral CT—initial experience. Radiology 217:564–571
10. Flohr T (2013) CT systems. Curr Radiol Rep 1(1):52–63
11. Flohr TG, Stierstorfer K, Ulzheimer S et al (2005) Image reconstruction and image quality evaluation for a 64-slice CT scanner with zflying focal spot. Med Phys 32(8):2536–2547
12. Primak AN, Giraldo JC, Eusemann CD, Schmidt B, Kantor B, Fletcher JG, McCollough CH (2010) Dual-source dual-energy CT with additional tin filtration: dose and image quality evaluation in phantoms and in vivo. AJR Am J Roentgenol 195(5):1164–1174
13. Chae EJ, Song JW, Seo JB, Krauss B, Jang YM, Song KS (2008) Clinical utility of dual-energy CT in the evaluation of solitary pulmonary nodules: initial experience. Radiology 249(2):671–681
14. International Commission on Radiological Protection (2007) The 2007 Recommendations of the International Commission on Radiological Protection. ICRP publication 103. Ann ICRP 37(2–4):1–332

15. Fazel R, Krumholz HM, Wang Y et al (2009) Exposure to low-dose ionizing radiation from medical imaging procedures. N Engl J Med 361(9):849–857
16. Committee to Assess Health Risks From Exposure to Low Levels of Ionizing, Radiation National Research Council of the National Academies (2006) Health risks from exposure to low levels of ionizing radiation: BEIR VII phase 2. National Academies Press, Washington, DC
17. Groves AM, Owen KE, Courtney HM et al (2004) 16-Detector multislice CT: dosimetry estimation by TLD measurement compared with Monte Carlo simulation. Br J Radiol 77:662–665
18. McNitt-Gray MF (2002) AAPM/RSNA physics tutorial for residents – topics in CT: radiation dose in CT. Radiographics 22:1541–1553
19. Brenner DJ (2006) It is time to retire the computed tomography dose index (CTDI) for CT quality assurance and dose optimization. Med Phys 33:1189–1191
20. Paterson A, Frush DP, Donnelly LF (2001) Helical CT of the body: are settings adjusted for pediatric patients? AJR Am J Roentgenol 176:297–301
21. Kalender WA (2011) Computed tomography. Wiley, New York
22. Gur D, Drayer BP, Borovetz HS et al (1979) Dynamic computed tomography of the lung: regional ventilation measurements. J Comput Assist Tomogr 3:749–753
23. Tajik JK, Tran BQ, Hoffman EA (1996) Xenon enhanced CT imaging of local pulmonary ventilation. Proc SPIE 2709:40–54
24. Marcucci C, Nyhan D, Simon BA (2001) Distribution of pulmonary ventilation using Xe-enhanced computed tomography in prone and supine dogs. J Appl Physiol 90:421–430
25. Kreck TC, Krueger MA, Altemeier WA et al (2001) Determination of regional ventilation and perfusion in the lung using xenon and computed tomography. J Appl Physiol 91(4): 1741–1749
26. Chon D, Simon BA, Beck KC et al (2005) Differences in regional wash-in and wash-out time constants for xenon-CT ventilation studies. Respir Physiol Neurobiol 148(1–2):65–83
27. Chae EJ, Seo JB, Goo HW, Kim N, Song KS et al (2008) Xenon ventilation CT with a dual-energy technique of dual-source CT: initial experience. Radiology 248(2):615–624
28. Chae EJ, Seo JB, Lee J et al (2010) Xenon ventilation imaging using dual-energy computed tomography in asthmatics: initial experience. Invest Radiol 45(6):354–361
29. Park EA, Goo JM, Park SJ et al (2010) Chronic obstructive pulmonary disease: quantitative and visual ventilation pattern analysis at xenon ventilation CT performed by using a dual-energy technique. Radiology 256(3):985–997
30. Thieme SF, Hoegl S, Nikolaou K et al (2010) Pulmonary ventilation and perfusion imaging with dual-energy CT. Eur Radiol 20(12):2882–2889
31. Simon BA (2005) Regional ventilation and lung mechanics using X-ray CT. Acad Radiol 12(11):1414–1422
32. Lachmann B, Armbruster S, Schairer W et al (1990) Safety and efficacy of xenon in routine use as an inhalational anaesthetic. Lancet 335:1413–1415
33. Hoag JB, Fuld M, Brown RH, Simon BA (2007) Recirculation of inhaled xenon does not alter lung CT density. Acad Radiol 14(1):81–84
34. Gattinoni L, Mascheroni D, Torresin A et al (1986) Morphological response to positive end-expiratory pressure in acute respiratory failure: computerized tomography study. Intensive Care Med 12:137–142
35. Gattinoni L, Pesenti A, Torresin A et al (1986) Adult respiratory distress syndrome profiles by computed tomography. J Thorac Imaging 1:25–30
36. Gattinoni L, Pesenti A, Bombino M et al (1988) Relationships between lung computed tomographic density, gas exchange and PEEP in acute respiratory failure. Anesthesiology 69: 824–832
37. Gattinoni L, Pelosi P, Pesenti A, Brazzi L, Vitale G, Moretto A, Crespi A, Tagliabue M (1991) CT scan in ARDS: clinical and physiopathological insights. Acta Anasthesiol Scand 95: 87–94

38. Gattinoni L, Pesenti A, Avalli L, Rossi F, Bombino M (1987) Pressure-volume curve of total respiratory system in acute respiratory failure. Computed tomographic scan study. Am Rev Respir Dis 136:730–736
39. Pelosi P, Crotti S, Brazzi L, Gattinoni L (1996) Computed tomography in adult respiratory distress syndrome: what has it taught us? Eur Respir J 9(5):1055–1062
40. Dougherty L, Asmuth JC, Gefter WB (2003) Alignment of CT lung volumes with an optical flow method. Acad Radiol 10:249–254
41. Dougherty L, Torigian DA, Affusso JD et al (2006) Use of an optical flow method for the analysis of serial CT lung images. Acad Radiol 13:14–23
42. Simon BA (2000) Non-invasive imaging of regional lung function using x-ray computed tomography. J Clin Monit Comput 16:433–442
43. Guerrero T, Sanders K, Noyola-Martinez J, Castillo E, Zhang Y, Thapia R, Guerra R, BorgheroY KR (2005) Quantification of regional ventilation from treatment planning CT. Int J Radiat Oncol Biol Phys 62:630–634
44. Guerrero T, Sanders K, Castillo E et al (2006) Dynamic ventilation imaging from four-dimensional computed tomography. Phys Med Biol 51:777–791
45. Castillo R, Castillo E, Martinez J et al (2010) Ventilation from four-dimensional computed tomography: density versus jacobian methods. Phys Med Biol 55:4661–4685
46. Yamamoto T, Kabus S, Klinder T et al (2011) Investigation of four-dimensional computed tomography-based pulmonary ventilation imaging in patients with emphysematous lung regions. Phys Med Biol 56:2279–2298
47. Yaremko BP, Guerrero T, Noyola-Martinez J et al (2007) Reduction of normal lung irradiation in locally advanced non-small-cell lung cancer patients, using ventilation images for functional avoidance. Int J Radiat Oncol Biol Phys 68:562–571
48. Vinogradskiy YY, Castillo R, Castillo E, Chandler A, Martel MK, Guerrero T (2012) Use of weekly 4DCT-based ventilation maps to quantify changes in lung function for patients undergoing radiation therapy. Med Phys 39(1):289–298
49. Fuld MK, Easley RB, Saba OI, Chon D, Reinhardt JM, Hoffman EA, Simon BA (2008) CT-measured regional specific volume change reflects regional ventilation in supine sheep. J Appl Physiol 104(4):1177–1184
50. Hogg JC, Nepszy S (1969) Regional lung volume and pleural pressure gradient estimated from lung density in dogs. J Appl Physiol 27(2):198–203
51. Coxson HO, Mayo JR, Behzad H, Moore BJ, Verburgt LM, Staples CA, Paré PD, Hogg JC (1995) Measurement of lung expansion with computed tomography and comparison with quantitative histology. J Appl Physiol 79(5):1525–1530
52. Salito C, Aliverti A, Gierada DS, Deslée G, Pierce RA, Macklem PT, Woods JC (2009) Quantification of trapped gas with CT and 3 He MR imaging in a porcine model of isolated airway obstruction. Radiology 253(2):380–389
53. Hedlund LW, Vock P, Effmann EL (1983) Evaluating lung density by computed tomography. Semin Respir Crit Care Med 5:76–87
54. Coxson HO, Rogers RM, Whittall KP, D'yachkova Y, Paré PD, Sciurba FC, Hogg JC (1999) A quantification of the lung surface area in emphysema using computed tomography. Am J Respir Crit Care Med 159(3):851–856
55. Salito C, Woods JC, Aliverti A (2011) Influence of CT reconstruction settings on extremely low attenuation values for specific gas volume calculation in severe emphysema. Acad Radiol 18(10):1277–1284
56. Aliverti A, Pennati F, Salito C, Woods JC (2013) Regional lung function and heterogeneity of specific gas volume in healthy and emphysematous subjects. Eur Respir J 41(5):1179–1188